

"This document is the unedited Author's version of a Submitted Work that was subsequently accepted for publication in ACS Applied Energy Materials, copyright © American Chemical Society after peer review. To access the final edited and published work see <https://pubs.acs.org/doi/full/10.1021/acsaem.1c01018>."

Incorporation of Activated Biomasses in Fe-N-C Catalysts for Oxygen Reduction Reaction with Enhanced Stability in Acidic Media

*Julia Müller-Hülstede^{*a, b}, Dana Schonvogel^a, Henrike Schmies^a, Peter Wagner^a, Alexander Dyck^c and Michael Wark^b*

^a Institute of Engineering Thermodynamics, German Aerospace Center (DLR), Carl-von-Ossietzky-Str. 15, 26129, Oldenburg, Germany; Institute of Chemistry,

^b Carl von Ossietzky University, Carl-von-Ossietzky-Str. 9-11, 26129, Oldenburg, Germany

^c Institute of Networked Energy Systems, German Aerospace Center (DLR), Carl-von-Ossietzky-Str. 15, 26129, Oldenburg, Germany

KEYWORDS

Non-PGM catalysts, ORR, Activated biomass, Stability, PEMFC

ABSTRACT

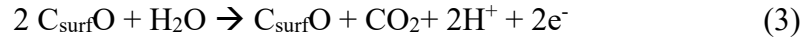
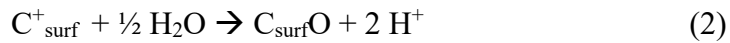
Fe-N-C materials are promising oxygen reduction reaction (ORR) catalysts for replacing expensive platinum-based catalyst (Pt/C) in proton exchange membrane fuel cells. However, they still show low volumetric activity and stability compared to Pt/C catalysts, with carbon corrosion being one of the main factors for the loss of active Fe-N_x sites. Within this study phosphoric acid activated rye straw and coconut shells are revealed as promising matrix for Fe-N_x sites with advanced stability against electrochemical carbon corrosion (5,000 cycles, 1.0-1.5 VRHE, 0.1 M HClO₄) compared to a common Fe-N-C catalyst based on carbon black. Electrochemical characterization of the two biomass-based catalysts (Fe-N-C_{Bio}) show on the one hand 50 % higher stability in terms of mass activity as well as comparable activity and active site density but on the other hand a lower selectivity towards the four-electron ORR compared to the common Fe-N-C catalyst. Nitrite stripping experiments in acetate buffer as electrolyte display 1.5-fold stronger effect of carboxylic acid adsorption than on common Fe-N-C catalyst, revealing differences to the electronic structure of Fe-N-C_{Bio} catalyst. This difference is mainly attributed to the presence of phosphor species and higher amounts of nitrogen functionalities in the Fe-N-C_{Bio} catalysts. The presence of P is assumed to stabilize the carbon against carbon corrosion by the inhibiting electron withdrawal from the C. This study points out the impact factors on Fe-N-C stability and further shows the promising application of activated biomasses in more stable and sustainable Fe-N-C catalysts for ORR.

1. INTRODUCTION

The proton exchange membrane fuel cell (PEMFC) is a key technology for the conversion of sustainable energy. However, for large-scale commercialization of PEMFCs, the durability has to

be increased and system costs need to be lowered.¹ One major cost factor is the Pt-based cathode material which is necessary to catalyze the sluggish oxygen reduction reaction (ORR). Thus, the reduction of Pt content in fuel cell electrodes is mandatory. For low temperature PEMFC decreased cathode loadings of around 0.1 mg_{Pt}/cm² are reported.^{1, 2} However, these low Pt-loadings lead to durability problems, so that Pt-based catalysts are limited either in costs or stability.¹ Therefore, non-precious metal catalysts (NPMC) are in the focus of current research.^{1, 3, 4} Within the last decades, the group of Me-N-C materials was identified as promising active ORR electrocatalysts in an acidic environment.⁴ In general, Me-N-C catalysts consist of ORR active atomic metal-nitrogen species (Me-N_x) which are incorporated into a graphitic carbon network. For the synthesis of these catalysts, pyrolysis of the carbon component, nitrogen- and metal precursors at temperatures in the range of 700-1000 °C is commonly carried out.⁵ Fe as metallic sites showed the highest ORR activity in acidic environment in comparison to other transition metals.⁶ However, there are two main challenges of Me-N-C catalysts to be overcome, namely a low stability and less volumetric activity in acidic electrolyte compared to Pt/C.^{3, 4, 7, 8} The latter leads to the requirement of high catalyst loadings and thick catalyst layers to achieve comparable performances to Pt/C catalysts, resulting in mass transport limitations during fuel cell operation.^{4, 8} To overcome these challenges, different optimization approaches to either tune the turnover frequency of single active sites or increase the active site density are under investigation.⁴ The low stability of Me-N-C catalysts is caused by different degradation processes being mainly demetallation, reversible surface oxidation and carbon corrosion.^{9, 10} Kumar *et al.* recently showed in load cycling experiments (0.6-1.0 V_{RHE}) of Fe-N-C catalyst in oxygen-saturated acidic electrolyte, that formed hydrogen peroxide is converted by the iron to reactive oxygen species which induce carbon corrosion and drastically decrease the mass activity by ~55 %.¹⁰ They further reported that

start/stop cycling in the range of 1.0-1.5 V in nitrogen- as well as in oxygen-saturated electrolyte also show significant decrease of 90 % in mass activity. The accelerated stress test (AST) conditions used in the study of Kumar *et al.* for start-stop cycling provoke electrochemical carbon corrosion. According to Ball *et al.* carbon corrosion of graphitic materials proceeds via three steps.¹¹ First the surface carbon is oxidized (eq. 1), followed by hydrolysis of surface and thus formation of oxidized species like hydroquinone/quinone, carboxylates or hydroxides (eq. 2). Finally, the oxidized surface is further reduced to carbon dioxide (eq. 3) leading to the loss of carbon matrix.^{11, 12}



If carbon neighbor atoms of Fe-N sites become oxidized forming e.g. hydroquinone/quinone species, steric and electronic effects can occur. This can lead to a hindered hydroperoxide dissociation during associative ORR mechanism on the Fe-N sites and thus to an increased hydrogen peroxide formation resulting in a lower selectivity towards ORR. Furthermore, the complete oxidation of carbon to CO₂ causes the detachment of selective Fe-N sites. The Me-N-C catalyst consists with up to 90-95 at% of carbon which partly host the active Fe-N_x sites, so that carbon corrosion can significantly influences the durability.^{3, 9, 13} Therefore, the research towards more stable Me-N-C catalysts, including the development of novel carbon supports is under intense research. As carbon components different commercial carbon blacks¹⁴, carbon nanotubes¹⁵ or graphene species¹⁶ and also the direct use of native biomasses¹⁷⁻²² were already investigated in Fe-N-C catalyst synthesis. The use of activated biomass-based carbons in Fe-N-Cs has not been

reported up to now. Chen *et al.* recently showed that activated biomasses are a promising cheap sustainable material group for electrocatalytic applications as they can have high porosity, graphitic structure and heteroatom doping.²³ Previous studies further showed the promising application of H₃PO₄, KOH or NaOH activated biomasses based on rice husks, coconut shells or wood sawdust as electrodes in supercapacitors²⁴, for wastewater treatment²⁵ or as metal-free ORR catalysts in alkaline electrolyte²⁶⁻²⁸. Furthermore, the studies of Wang *et al.*²⁶ and Borgehei *et al.*²⁷ performed stress tests of N- and P-doped carbons using potential cycling (1000 cycles, -1.2-0.2 V_{Ag/AgCl}) and chronoamperometry (13 h, -0.3 V_{Ag/AgCl}) in alkaline electrolyte. They revealed that natural heteroatom content is beneficial for a higher electrochemical stability. On the basis of these findings, the application of activated biomasses in Fe-N-C catalysts has great potential. In our previous study, we have recently demonstrated that phosphoric acid activated rye straw results in a mesoporous carbon support with a moderate surface area of 800 m²/g which is a beneficial carbon support for successful Fe-N site incorporation, whereas KOH-activated carbon from rye straw is not applicable for atomic Fe-N_x site incorporation.²⁹

Thus, in this study, rye straw and coconut shells are activated by phosphoric acid, used as carbon matrix for Fe-N-C synthesis and applied as ORR catalysts in acidic electrolyte. The electrochemical activity, selectivity, turnover frequency and site density of the novel biomass-based catalysts and a common Black Pearl[®]-based Fe-N-C catalyst are compared and related to the physical properties of the different materials. Furthermore, higher stability against electrochemical carbon corrosion for the activated biomass-supported Fe-N-C catalysts is shown.

2. EXPERIMENTAL SECTION

2.1. Activation of biomass

Activation of coconut shells and rye straw was adapted from Koyutürk *et al.*³⁰ 300 mg of coconut shell powder (COCONIT 300, Mahlwerk Neubauer-Friedrich Geffers) or minced rye straw were impregnated with 1.5 g H₃PO₄ (≤ 85 % Carl Roth. p.a.). After two days drying in vacuum oven at 30 °C, the impregnated biomass was heated up to 580 °C with 5 °C min⁻¹ and hold for 3 h under nitrogen flow of 100 mL min⁻¹ in a steel tube furnace, followed by a washing step with 0.5 M HCl (p.a. VWR) and water until neutral pH and drying in vacuum oven at 150 °C for 2 days. Due to a moderate oxygen content (> 10 at%) no additional oxidation step was carried out for the biomass-based carbons.

2.2. Oxidation of commercial carbon support

Commercial carbon support Black Pearls® 2000 (Cabot) were oxidized previous to use according to literature, to generate oxygen functionalities which decompose during Fe-N-C synthesis to form defect sites for enhanced N incorporation.³¹ 2 g of Black Pearls® were stirred in concentrated HNO₃ (200 mL, 65 % Carl Roth) for 5 h, followed by washing with water until neutral pH and drying in vacuum oven at 30 °C.

2.3. Fe-N-C synthesis

The synthesis of Fe-N-C catalyst was according to common procedures reported in literature.³²⁻
³⁴ The carbon powder (100 mg) was impregnated with 16.25 mg iron(II)acetate (Sigma Aldrich) and 421 mg cyanamide (Sigma Aldrich) with 4 mL ethanol (Carl Roth). The dispersion was stored in a sonication bath until complete evaporation of ethanol and dried in vacuum oven over night at

30 °C. A first pyrolysis was carried for 1 h at 900 °C with 5 °C min⁻¹ and 100 L h⁻¹ nitrogen flow in a ceramic tube furnace followed by acid leaching with 2 M H₂SO₄ (Carl Roth) for 16 h. Finally, the catalyst powder was washed with water until neutral pH and after drying a second pyrolysis at 900 °C for 1 h was performed.

2.4. Physical characterization

For transmission electron microscopy (TEM) the catalyst powder was dispersed in ethanol, and 5 µL were deposited on a polyvinyl formal coated copper grid with 200 meshes (Plano). The images were taken with an EM902A (Zeiss) with 80 kV acceleration voltage. High-resolution TEM images coupled with an energy dispersive x-ray spectrometer (EDS) were taken with the JEM-2100F (Jeol) device using 200 kV accelerating voltage and the INCA software with 250 X-Max80 SDD detector from Oxford instruments. For powder X-ray diffraction (XRD) measurements an Empyrean series 2 (PANalytical) with Cu K_α radiation at 40 kV and 40 mA in Bragg-Brentano mode and HighScore Plus software were used. The X-ray photoelectron-spectra (XPS) were recorded with ESCALAB 250Xi (Thermo Fisher) with Al K_α radiation. High resolution spectra were recorded with a pass energy of 20 eV, dwell time of 50 ms and step size 0.02 eV. Nitrogen sorption was carried out with TriStar II 3020 (Micromeritics GmbH, Germany). Inductively coupled plasma mass spectrometry (ICP-MS) was performed using XSeries2 (Thermo Fisher Scientific) by use of scandium as internal standard (Carl Roth) and Fe concentrations in range of 500-5000 µg L⁻¹ (Carl Roth) for calibration solutions. Sample preparation was according to literature.³⁵ 15 mg of catalyst were mixed with 2 mL of concentrated HNO₃ (Rotipuran® Supra Carl Roth) for 1 h at 100 °C, followed by filtration and preparation of a 50 mL solution using 2 % HNO₃.

2.5. Electrochemical measurements in perchloric acid

Electrochemical characterization was carried out using an Autolab potentiostat (Metrohm) and 0.1 M HClO₄ (Sigma Aldrich) as electrolyte. A glass cell assembled with a reversible hydrogen electrode (RHE) as reference electrode (RE), that was calibrated prior to use, and a Pt-wire or graphite rod as counter electrode (CE) was used. CE and RE were separated from the WE with porous glass frits to prevent contaminations like carbonaceous materials. Influence of the Pt CE on the experiment was excluded through additional reference measurements with a graphite rod as CE for each catalyst and is further discussed in the supporting information. As working electrode (WE) a rotating-ring disk electrode (RRDE, Pine, area of 0.2472 cm²) with Pt-ring and glassy carbon (GC) disc was used. The catalyst ink was fabricated by mixing 6 mg of catalyst powder, 561.6 μ L water, 126 μ L 2-propanol and 76.2 μ L of a 5 wt% Nafion[®] solution in a mixture of lower aliphatic alcohols and water (Sigma Aldrich) via 15 min of bath-sonication (Brandelin electronic) followed by 4 min of horn-sonication (Branson Digital Sonifier, amplitude 10 %). The GC disc was coated with 12.6 μ L (400 μ g cm⁻²) of catalyst ink, dried at 60 °C in oven for 6 min and stored with a droplet of water until use. The electrolyte was saturated with either nitrogen or oxygen for 20 min prior to measurements. In general, the measurements started with three cyclic voltammograms (CVs) in oxygen-saturated electrolyte at 1600 rpm in the range of 0.05-1.05 V with a scan rate of 5 mV s⁻¹ and an applied ring potential of 1.2 V. Afterwards, the same procedure was carried out in nitrogen-saturated electrolyte for capacitive current correction. For correction of polarization curves by the electrolyte resistance, electrochemical impedance spectroscopy in a range of 100 kHz-0.1 Hz at 0.3 V was recorded. Afterwards, five CVs in the range of 0.05-1.0 V with 50 mV s⁻¹ were recorded. An accelerating stress test protocol adapted from the Fuel Cell Commercialization Conference of Japan (FCCJ)³⁶ was used to provoke electrochemical carbon

corrosion which can occur during start stop process of fuel cell systems or anode starvation. In detail, 5,000 cycles in nitrogen-saturated electrolyte in the range of 1.0-1.5 V with a scan rate of 500 mV s⁻¹ were applied, followed by final characterization analog to initial measurements. For each catalyst three measurements were performed. For data evaluation, the Koutecky-Levich eq. 4 was used to calculate kinetic current density j_{kin} using the current density j at 0.75 V and 0.80 V and the limiting current density in the range of 0.1-0.4 V. The mass-specific activity (MA) was calculated using the mass of catalyst on the electrode $m_{catalyst}$ (eq. 5).

$$j_{kin} = \frac{j \cdot j_{lim}}{j_{lim} - j} \quad (4)$$

$$MA = \frac{j_{kin}}{m_{catalyst}} \quad (5)$$

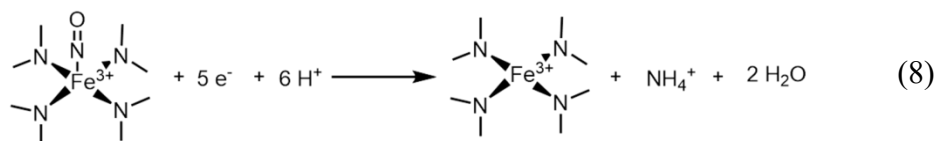
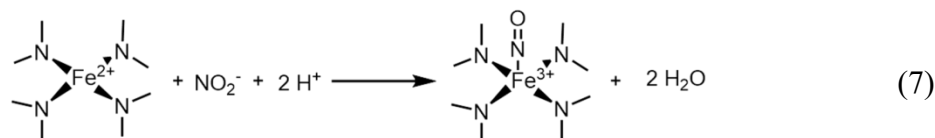
The onset potentials were determined according to literature from the polarization curves recorded in oxygen-saturated electrolyte at a current density of -0.1 mA cm⁻².³⁷ The hydrogen peroxide yield was calculated according to eq. 6, using disc current density j_{Disk} , ring current density j_{Ring} and ring electrode specific collection efficiency N (0.37, supplied by Pine Instruments).

$$\text{Yield X H}_2\text{O}_2 = \frac{200 \cdot j_{Ring}}{(N \cdot j_{Disk}) + j_{Ring}} \quad (6)$$

2.6. Electrochemical measurements in acetate buffer

The nitrite stripping experiments were carried out according to Malko *et al.*³⁸ using 0.5 mol L⁻¹ acetate buffer as electrolyte which was prepared using glacial acetic acid (VWR) and sodium acetate (Sigma Aldrich). Catalyst loading was the same as in RRDE experiments in HClO₄

(400 $\mu\text{g cm}^{-2}$) to ensure that the electrode is completely covered by catalyst. The same glass cell and frits were used as for measurements in HClO_4 . A freshly prepared and calibrated RHE was used as reference electrode and a graphite rod was taken as counter electrode. Detailed measurement procedure including electrode cleaning/activation procedure, fresh measurements, poisoning, stripping and recovered measurements can be found in literature.³⁸ For each catalyst three electrodes were coated and measured. In general a nitrite ion adsorbs onto the active Fe site (eq. 7) forming a nitrosyl complex.³⁸ By applying a potential lower than 0.3 V vs. RHE the species is then reduced by 5 electrons to form an ammonium ion and recover the iron (III) site (eq. 8).³⁸ In a further reduction the iron(III) can also be reduced to Fe (II) species.³⁹



The stripping charge Q_{Strip} was calculated by dividing the area between poisoned and recovered baseline scan by the scan rate of 5 mV s^{-1} and the total catalysts mass on the electrode. The Q_{Strip} was used for calculation of mass-based site density SD_{Mass} in eq. 9, assuming an electron transfer number n_{Strip} of 5 (see eq. 8). By using the surface area (SA) also the area-based site density SD_{Area} can be determined (eq. 10).³⁸

$$SD_{\text{Mass}}[\text{sites g}^{-1}] = \frac{Q_{\text{Strip}} [\text{C g}^{-1}] \cdot N_{\text{A}} [\text{mol}^{-1}]}{n_{\text{strip}} \cdot F [\text{C mol}^{-1}]} \quad (9)$$

$$SD_{Area} [\text{sites nm}^{-2}] = \frac{Q_{Strip} [\text{C g}^{-1}] \cdot N_A [\text{mol}^{-1}]}{n_{strip} \cdot F [\text{C mol}^{-1}] \cdot SA [\text{nm}^2 \text{ g}^{-1}]} \quad (10)$$

For determination of the TOF, the differences in kinetic activity ΔI_{kin} at 0.8 V before and after poisoning was calculated by using eq. 4 and the polarisation curves of nitrite stripping experiment. The ΔI_{kin} value as well as Faraday constant F and SD_{mass} was used in eq. 11 for calculation of TOF.³⁸

$$TOF(@0.8 \text{ V}) [\text{s}^{-1}] = \frac{\Delta I_{kin} [\text{A g}^{-1}]}{F [\text{C mol}^{-1}] \cdot SD_{mass} [\text{mol g}^{-1}]} \quad (11)$$

3. RESULTS AND DISCUSSION

Three Fe-N-C catalysts were fabricated, one based on oxidized commercial Black Pearls[®] (Fe-N-ox-BP) and two catalysts based on phosphoric acid activated rye straw (Fe-N-aRS) and coconut shell (Fe-N-aCoco). The detailed physical characterization of the Fe-N-ox-BP and Fe-N-aRS catalyst, can be found in our previous publication.²⁹ In this study, appropriate physical characterization of the three materials are presented and discussed within the scope of their electrochemical behaviour.

3.1. Elemental composition and morphology of Fe-N-C catalysts

For evaluation of the catalyst's morphology and elemental distribution high-resolution transmission electron microscopy with energy dispersive spectroscopy (HR-TEM/EDS) was carried out. Figure 1 (a)-(c) shows TEM images of the three catalysts and indicates larger agglomerate sizes for the biomass-based catalysts Fe-N-aRS and Fe-N-aCoco than for Fe-N-ox-BP. This was expected as the production of biomass-based carbons is a top-down approach

compared to the bottom-up approach of carbon blacks which are commonly produced by thermal cracking of hydrocarbons.⁴⁰ Especially the Fe-N-aRS catalyst shows larger particles up to the micrometer region which might be due to larger initial biomass size being small pieces (millimetre range) instead of fine powder (micrometer range) in case of the coconut shell. Qualitative EDS mapping of Fe and N in Figure 1 (d)-(f) displays uniform distribution of N and Fe over the carbon supports. Only for the Fe-N-ox-BP two small Fe particles are observed besides the uniform distribution. This confirms that besides rye straw²⁹ also the phosphoric acid activation of other biomasses like coconut shells can be assumed as an appropriate carbon matrix for atomic Fe and N incorporation. Furthermore, the diffractograms in Figure 1 (g) show no reflexes which can be assigned to metallic Fe or carbide species. This underlines that the two Fe-particles observed for Fe-N-ox-BP catalyst in EDS mapping are negligible. Besides the characteristic signals for graphitic carbons at 25 ° and 44 ° assigned to (002) and (011) plane (ICDD:98-061-7290) the activated biomass catalysts show additional sharp low intensity reflexes in the region between 20 ° and 40 ° with two more pronounced peaks at 20 ° and 26 °. These peaks might be due to residual phosphoric species from the activation step as also observed in the native H₃PO₄-activated biomasses²⁹ and in other studies dealing with H₃PO₄ activation.^{25, 41, 42} These peaks were not further discussed in literature and identification through data bank was not successful. However, the attribution of the peaks to phosphor species is further supported by the XPS results, which show only the presence of N, C, Fe and P in the biomass-based Fe-N-Cs. For P an amount of 1.9-2.2 at% was detected (Table 1). The phosphor in the biomass-based catalysts can be present as red phosphorous, phosphates or chemically bonded forms like –C-P- or C-O-P species.⁴³ P-atoms might also be incorporated into the graphitic carbon network. Phosphorous compounds can additionally be encapsulated by the carbon as the H₃PO₄ activation is a sol-gel type

carbonization.³⁰ However, it is also reported that substitution of C by P atoms is rather uncommon as the π -conjugation with a graphene plane is not coplanar.^{43, 44} Therefore, the bonded forms (-C-P, C-O-P) seem to be more likely present in the activated biomass. The presence of P on the C-matrix inhibits electron withdrawal from the carbon and therefore can have a stabilizing effect on the electronic carbon.⁴³

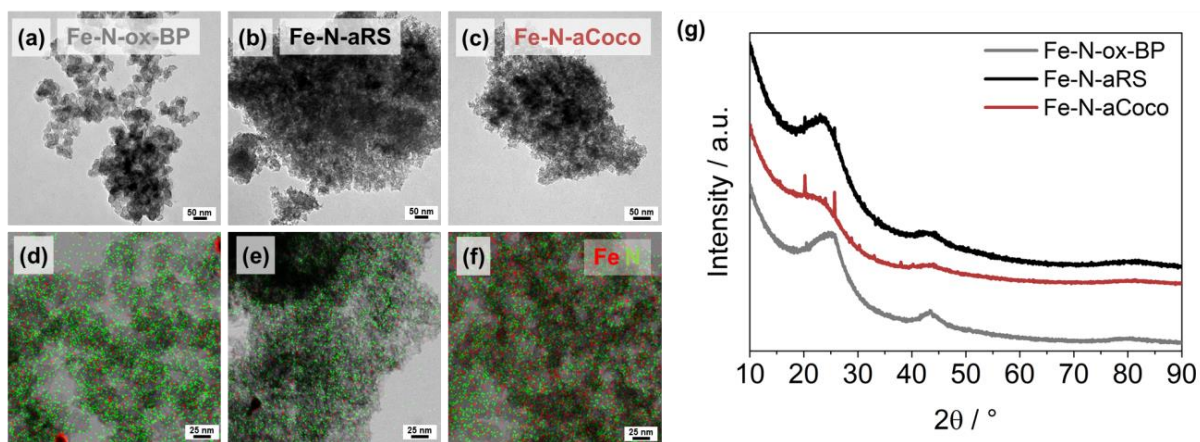


Figure 1. TEM images (top) and EDS mapping of Fe and N (bottom) for Fe-N-ox-BP (a, d), Fe-N-aRS (b, e) and Fe-N-aCoco (c, f) as well as powder X-ray diffractograms of the catalysts (g).

The near-surface elemental analysis by XPS listed in Table 1 (spectra in SI Fig. S1 and partly in ref.²⁹) shows higher oxygen and also nitrogen contents for the biomass-based catalysts. The surface nitrogen content of the native activated biomasses determined by XPS is 2.5 at% for aRS²⁹ and 2.3 at% for aCoco, which can be the reason for higher total nitrogen content in the biomass-based Fe-N-Cs. Furthermore, the phosphor can promote the nitrogen incorporation as reported by Choi *et al.*⁴⁵ Especially, the amount of pyridinic, graphitic and pyrrolic N of both biomass-based catalysts, which can have an influence on stability and selectivity during ORR, is higher compared to the carbon black-based catalyst (Table 1). Pyrrolic N is known to be more unselective towards the preferred 4e⁻ ORR pathway and can instead form hydrogen peroxide through a 2e⁻ oxygen

reduction.⁴⁶ Due to the low signal to noise ratio in the Fe2p spectra no proper peak fitting was carried out and therefore no Fe-N₄ site was fitted into the N1s spectra. However, the Fe-N_x species might be attributed to the pyridinic N peak.⁴⁶ Furthermore, the bulk iron contents were determined by ICP-MS resulting in comparable Fe ratios being 1.33 wt% Fe for Fe-N-ox-BP²⁹, 1.29 wt% for Fe-N-aCoco and 1.20 wt% for Fe-N-aRS²⁹. This indicates that the differences in carbon matrix have no effect on the amount of incorporated iron.

Table 1. Near-surface elemental content of common Fe-N-ox-BP and biomass-based Fe-N-aRS taken from previous study²⁹ and Fe-N-aCoco catalysts including the detailed percentage of N-functionalities in at%.

		Fe-N-ox-BP ²⁹	Fe-N-aRS ²⁹	Fe-N-aCoco
Surface composition / at% (XPS)	C1s	91.2	78.2	78.2
	O1s	2.4	9.0	10.6
	P2p _{3/2}	0.0	2.2	1.9
	Fe2p _{3/2}	0.4	0.4	0.3
	N1s	6.0	10.3	9.1
	Pyridinic N	2.3	3.3	3.0
	Pyrrolic N	0.9	2.0	2.1
	Graphitic N	2.1	3.9	3.2
	Nitroxide	0.7	1.1	0.8

Next to morphology and elemental content of the catalysts, surface area and porosity can impact the catalyst performance. Therefore, nitrogen sorption experiments were carried out. The Brunauer-Emmett-Teller surface areas (S_{BET}) and micropore volumes of Fe-N-ox-BP

(1,280 m² g⁻¹, 1.19 cm³ g⁻¹) and Fe-N-aRS (977 m² g⁻¹, 0.875 cm³ g⁻¹) are discussed in detail in our previous study (SI Fig. S2 and Table S1).²⁹ The Fe-N-aCoco catalyst shows a comparable isotherm shape (SI Fig. S2) and values to the other catalysts with a surface area of 1,117 m² g⁻¹ and a total pore volume of 0.835 cm³ g⁻¹, resulting mainly from mesopores, as the micropore volume is only 0.27 cm³ g⁻¹. This demonstrates a successful synthesis of catalysts based on different carbon sources with comparable porosity. Summarizing the physical properties, main differences between biomass-based Fe-N-C catalysts and common Black-Pearl[®]-based Fe-N-C catalyst are the particle size and heteroatom doping.

3.2. Electrochemical activity, selectivity and stability

The electrocatalytic performances of the catalysts were evaluated using a rotating ring-disc electrode (RRDE) setup in 0.1 M HClO₄ electrolyte. The ORR polarization curves in Figure 2 (a) were used to determine the limiting current density j_{lim} and current densities j at potentials of 0.75 V and 0.80 V, respectively, for calculation of the mass activity before and after an AST. The results after the AST will be discussed separately. With a look to the initial mass activities at 0.75 V displayed in Figure 2 (c), comparable values of 5.24 ± 0.55 A g⁻¹ and 5.19 ± 0.44 A g⁻¹ for Fe-N-ox-BP and Fe-N-aCoco can be observed. The Fe-N-aRS catalyst, on the other hand, reveals a slightly lower mass activity of 4.17 ± 0.36 A g⁻¹, which is due to the influence of diffusion limitations. The mass activities calculated at 0.8 V ranging between 1.3-1.6 A g⁻¹ for the biomass-based catalysts being higher compared to Fe-N-ox-BP with a MA value of 1.08 ± 0.13 A g⁻¹. For investigation of the influence from the Pt-counter electrode on the mass activities, a freshly coated electrode of each catalyst was measured with a graphite rod as counter electrode analogous to the other measurements. The polarization curves measured with a graphite rod as counter electrode are shown in Figure 2 (b) and the calculated mass activities are marked in Figure 2 (c). The

comparison of measurements with different counter electrodes reveals highly comparable mass activity losses. Thus, the Pt counter electrode does not influence the mass activity in this study in terms of an increased mass activity or stability due to unwanted Pt-deposition on the catalyst.

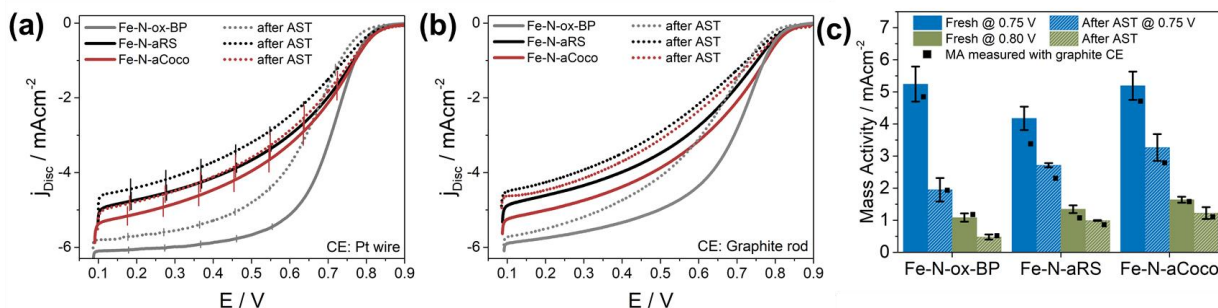


Figure 2. Mean geometric disc current density j_{Disc} of anodic scan under oxygen-saturated electrolyte with 1600 rpm before and after AST (N_2 -saturated electrolyte, 5000 cycles, 1.0-1.5 V) out of three independent AST measurements with indicated error bars, measured with a Pt-wire as counter electrode (CE) (a) and with a graphite rod as CE (b) and calculated mass activity using current densities at 0.75 V and 0.80 V before and after AST with a catalysts loading of $400 \mu\text{g}/\text{cm}^2$ (c).

While the kinetic region in polarisation curve is comparable for the three catalysts indicating similar intrinsic activities, the comparison of the polarization curves at lower potentials in the range of 0.1-0.5 V shows lower diffusion-limiting current densities for the biomass-based catalysts. This is attributed to the larger particle sizes of the biomass-based carbons (Figure 1). Furthermore, surface roughness as well as aggregate formation of the catalyst particle on the electrode is reported to negatively impact the limited current.⁴⁷ This could be the case for the biomass-based catalysts which showed larger aggregate size in TEM images. Especially, the Fe-N-aRS catalyst with largest particles in Figure 1 displays the lowest diffusion-limited current in Figure 2. However, also the

selectivity for ORR can impact the limited current density. If less than $4e^-$ are generated per O_2 molecule the diffusion-limited current decreases.⁴⁸ The selectivity was analyzed by collecting the ring current density j_{Ring} presented in Figure 3 (a).

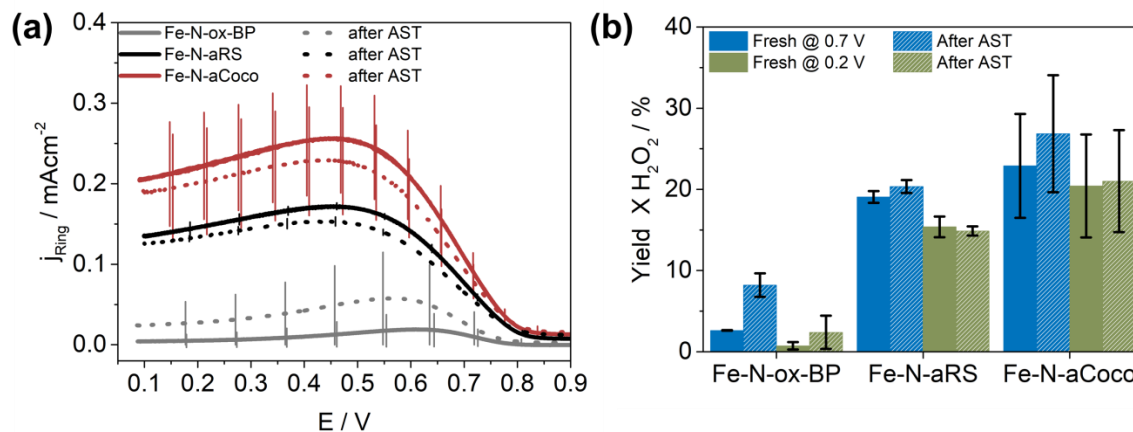


Figure 3. Ring current densities before and after AST (a) and hydrogen peroxide yield determined at 0.2 V and 0.7 V (b) before and after AST with error bars out of three measurements.

The j_{Ring} values are significantly higher for the biomass-based catalysts compared to Fe-N-ox-BP indicating lower selectivity. This is besides the particle size the second reason for lower diffusion-limited current densities in ORR polarization curves (Figure 2). The hydrogen peroxide yields are calculated at two different potentials, 0.2 V and 0.7 V, and displayed in Figure 3 (b). In the case of the Fe-N-ox-BP catalyst, yields lower than 3 % H_2O_2 are observed, whereas the biomass-based catalysts show higher values in the range of 15-30 %, indicating a significantly lower selectivity towards the 4 electron ORR pathway. This can originate from the higher content of nitrogen species being in case of Fe-N-aCoco 52 % and in case of Fe-N-aRS 72 % higher than for Fe-N-ox-BP (Table 1). Especially pyrrolic nitrogen is known to catalyze the formation of hydrogen peroxide causing a lower selectivity.^{46, 49} Furthermore, pyridinic nitrogen is known to further reduce hydrogen peroxide to water within a 2 electron process.^{46, 49} Artyushkova *et al.*

reported that a larger ratio of pyridinic to pyrrolic nitrogen species indicates lower yields of hydrogen peroxide.⁴⁶ This was also found for the catalysts in this study. For Fe-N-ox-BP a ratio of pyridinic to pyrrolic nitrogen of 2.6 was calculated, whereas lower values were found for Fe-N-aCoco being 1.4 and for Fe-N-aRS being 1.7. Choi *et al.* reported that P-species in carbons have no negative impact on the selectivity. They compared N-doped carbons with P- and N-doped carbons and found that addition of P has a rather positive impact on the selectivity.⁴⁵ Therefore, the lower selectivity of the biomass-based carbons in this study is assumed to completely originate from the nitrogen species. Furthermore, ORR-measurements of the P-species containing biomass (aRS) shows very low ORR activity which is comparable to activity of ox-BPs. (Figure S3).

Further analysis of electrochemical data was carried out, using the Tafel plot which is shown in Figure 4. The calculation of Tafel slope can be used for estimation of mechanistic properties like the rate-determining step during the ORR.⁵⁰ At low overpotentials, occurring at electrode potentials < 0.79 V, a linear trend can be observed and Tafel slopes were calculated, whereas at higher overpotentials the linear trend is not clearly given anymore. This observation is similar to that observed for several other common Me-N-C catalysts in literature.⁵¹ For Fe-N-ox-BP a Tafel slope of 69 ± 2 mV dec⁻¹ was calculated and for the biomass-based catalysts a value of around 81 ± 5 mV dec⁻¹ was determined (Table 2). All values are comparable to Tafel slopes of other Fe-N-C catalysts in literature⁵²⁻⁵⁴ The variation of reported Tafel slopes in the range of 60-80 mV dec⁻¹, also found in literature, can be due to different intermediate coverages during associative ORR mechanism which significantly influence the Tafel slope.^{50, 54}

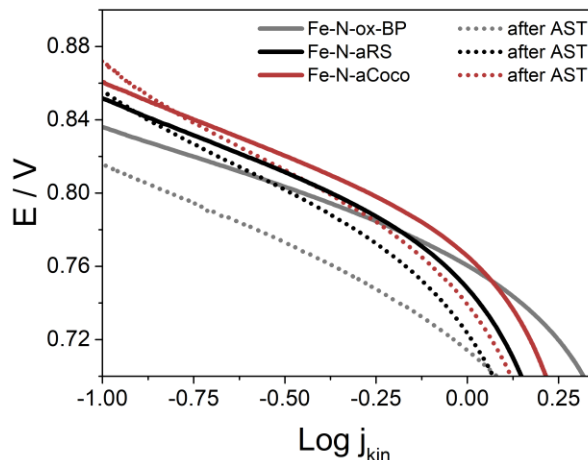


Figure 4. Tafel plots before and after AST of Fe-N-ox-BP, Fe-N-aCoco and Fe-N-aRS.

Next, the electrochemical stability of the catalysts will be discussed. An accelerated stress test including 5,000 cycles between 1.0 V and 1.5 V in N₂-saturated electrolyte with a scan rate of 500 mV s⁻¹ was performed. This test electrochemically provokes carbon corrosion, which becomes significant at potentials higher than 1.1 V⁵⁵ and is known to be one of the main reason for Fe-N-C catalyst degradation.^{13, 56-58}

The ORR polarization curves and the calculated mass activities after AST in Figure 2 display a decrease in activity for all catalysts. The relative mass activity loss is listed in Table 2 and shows a significantly lower loss for the biomass-based catalysts. An up to 50 % better stability is given for these materials. This is also in accordance with the onset potentials in Table 2, which show no significant change for biomass-based catalysts, whereas the Fe-N-ox-BP catalyst shows a decrease of 21 mV. The polarization curves in Figure 2 further show a decrease in diffusion limited currents, which can be assigned to a loss in 4 electron ORR selectivity.⁵⁹ However, the Fe-N-aCoco and Fe-N-aRS catalyst show only small increases in hydrogen peroxide yield after AST in Figure 3 by factor 0.03-0.17, which is nearly within the error bars. These negligible

changes in selectivity are in accordance to the low decrease of mass activity compared to the Fe-N-ox-BP catalyst. The Fe-N-ox-BP catalyst, on the other hand, shows an increase of the hydrogen peroxide yield by factor 2.28. Although the H_2O_2 yield of Fe-N-ox-BP is still lower after AST compared to the biomass-based catalysts, the increase indicates a loss of selective ORR sites like Fe-N₄ being in agreement with the higher loss in mass activity compared to the biomass-based Fe-N-C catalysts.

For further analysis of degradation behavior and changes in ORR mechanism Tafel slopes after AST can be analyzed. For all three catalysts an increase in Tafel slope to values between 117 and 131 mV dec^{-1} is observed as displayed in Table 2. This increase can be attributed to a change in the rate-determining step meaning that the first electron transfer forming -OOH species becomes the rate-determining step as explained by Choi *et al.* who also observed change in Tafel slope from $\sim 63 \text{ mV dec}^{-1}$ to 110 mV dec^{-1} after treatment of Fe-N-C with H_2O_2 .⁹ This change is induced by the partial oxidation of the carbon matrix leading to an oxygenated surface.⁵⁹ The changes in Tafel slope are comparable for all three catalysts, indicating similar changes in ORR mechanism or rather oxygenation of surface for all three catalysts through AST.

Table 2. Overview of mass activity loss determined at 0.75 V and 0.80 V, onset potential and Tafel slope before and after AST of biomass- and Black Pearls[®]-based Fe-N-C catalysts.

	MA loss / %		Onset Potential / V		Tafel slope at low overpotentials ($E \geq 0.79$ V) / mV dec^{-1}	
	at 0.75 V	at 0.8 V	Before AST	After AST	Before AST	After AST
Fe-N-ox-BP	63 ± 3	56 ± 3	0.840 ± 0.004	0.821 ± 0.005	69 ± 2	117 ± 12
Fe-N-aRS	35 ± 5	26 ± 5	0.852 ± 0.002	0.853 ± 0.003	81 ± 3	121 ± 8
Fe-N-aCoco	37 ± 3	25 ± 6	0.859 ± 0.003	0.871 ± 0.005	81 ± 5	131 ± 10

The change of carbon materials after AST can further be evaluated through cyclic voltammetry in nitrogen-saturated electrolyte (Figure 5). Before AST no sharp peaks which can be correlated to redox transition of $\text{Fe}^{2+}/\text{Fe}^{3+}\text{-N}_x$, which are typically found in the range of 0.64-0.78 V, were observed.⁶⁰⁻⁶³ As reported in literature this $\text{Fe}^{2+}/\text{Fe}^{3+}\text{-N}_x$ redox peaks can be superimposed by the double layer capacity and furthermore, the observation of this redox peak is not correlating to the catalyst's activity.^{58, 60} The biomass-based catalysts show rather a broad peak over the whole potential range which can be assigned to oxygen functionalities like hydroquinone/quinone redox species that can be more pronounced for the biomass-based catalysts due to higher amount of oxygen. The capacities of the materials, determined at 0.2 V of the anodic scan, show the smallest double layer capacity for Fe-N-ox-BP catalyst with a value of $50 \pm 5 \text{ mF cm}^{-2}$, whereas for the biomass-based catalysts higher double layer capacities were observed, being $67 \pm 7 \text{ mF cm}^{-2}$ for Fe-N-aRS and $83 \pm 11 \text{ mF cm}^{-2}$ for Fe-N-aCoco, respectively. (see SI Table S2). The double layer capacity can be related to surface area, porosity, electrical conductivity and surface

hydrophilicity.^{12, 64} The surface area of the biomass-based catalysts is lower compared to the Fe-N-ox-BP catalysts (SI Table S1), so that the higher double layer capacitance must be related to the larger amount of oxygen functionalities in Fe-N-aRS and Fe-N-aCoco. This is in accordance to the observation of small hydroquinone/quinone peaks and the higher amount of surface-oxygen which was determined by XPS being 9.0 at% for Fe-N-aRS and 10.6 at% for Fe-N-aCoco and only 2.4 at% for Fe-N-ox-BP. Oxygen-functionalities can lead to an increased hydrophilic surface and thus increases the affinity between the aqueous electrolyte and catalyst surface leading to higher double layer capacity.⁶⁵

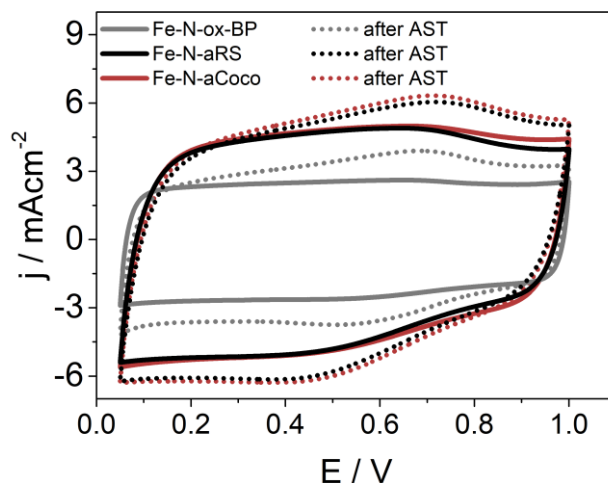


Figure 5. Cyclic voltammograms of Fe-N-ox-BP, Fe-N-aRS and Fe-N-aCoco before and after AST.

After the AST for all catalysts an increase in capacity due to the formation of surface functional oxygen groups or pores is observed, indicating oxidation of carbon surface (eq. 2).⁶⁶ This is further evidenced by the appearance of a broad hydroquinone/quinone redox couple with peak maximum at around 0.7 V for all catalysts.⁶⁴ These results are in accordance to the comparable changes in Tafel slopes (Figure 4, Table 2) which also shows oxygenation of the catalyst's surface. As all

three catalysts show similar changes, the differences in stability in terms of mass activity cannot directly related to the carbon itself, but rather to the stabilization of Fe-N_x sites. The lower stability of the selective Fe-N_x sites of Fe-N-ox-BP is indicated by the significant increase in H₂O₂ yield (Figure 2). A higher durability of the Fe-N_x sites can have different origins. One reason could be the iron site itself, which can be more stable. Li *et al.* recently reported that the Fe-N₄ site can be divided into two ORR active sites, being a high-spin Fe(III)-N_x and a low- or medium-spin Fe(II)-N_x site, determined by density function theory (DFT) calculation and Mössbauer spectroscopy.⁶⁷ While the latter site was shown to be durable during fuel cell operation, the high-spin site formed iron oxide particles. The higher stability of the low- or medium spin Fe(II)-N_x site was assumed to have reasons like less formation of reactive oxygen species, a higher graphitic environment or a subsurface position leading to activation of N-doped surface.⁶⁷ In our study, the synthesis parameter like precursors and temperature are similar for all three catalysts, so that differences in active sites can rather be attributed to differences in surface doping, carbon morphology and carbon porosity. First, the pore structure of the biomass-based catalysts shows smaller mesopores compared to Fe-N-ox-BP. This was observed by the hysteresis during the N₂-sorption experiments (SI Fig. S2). Thus, active sites in the biomass-based catalysts might be hosted in these smaller pores compared to Fe-N-ox-BP. Second, a difference in electronic carbon structure was also observed through the higher amounts of N- and P-species for Fe-N-aRS and Fe-N-aCoco catalyst. The phosphor present in the activated biomass can increase the electrochemical carbon stability near to the embedded Fe-N_x sites. Wang *et al.* reported that P-species inhibit the electron withdrawal from the carbon.⁴³ This can also impact the electrochemical induced carbon oxidation near the active sites during the AST and lead to higher stability of Fe-N_x sites which are incorporated near to P-species or also N-species. Furthermore, nitrogen doping and especially the

presence of pyrrolic N species is reported to increase the resistance towards carbon corrosion.³¹ Pyrrolic-, pyridinic- and graphitic-N can lead to instable intermediates of surface oxides during carbon corrosion mechanism and thus to an increase of the stability.⁶⁸ For further analysis of stability, identical location TEM was carried out for the Fe-N-ox-BP catalyst, because this catalyst showed the highest MA loss after the AST. Through IL-TEM it is possible to observe the same location before and after AST. However, no change in carbon morphology or rather particle redeposition was observed (SI Fig. S4).

3.3. Evaluation of site density and turnover frequency

To further study differences in active sites of the catalysts in terms of site density and turnover frequency (TOF), nitrite stripping experiments introduced by Malko *et al.* were performed.³⁸ In contrast to ex-situ measurements like CO cryo sorption or Mössbauer spectroscopy, the nitrite stripping experiments allow the determination of surface sites which are electrochemical active. Although it is reported that the active sites determined by the nitrite stripping are underestimated as not all sites are affected or reached by the nitrite^{35, 69}, the values will be used for a relative comparison of the catalysts in this study. In general, the Fe-N_x is poisoned by a nitrite molecule, which can be monitored by recording ORR polarisation curves before and after poisoning to observe a decrease in ORR activity. In a further step, the nitrite ions are electrochemically reduced to ammoniums ion by applying potentials lower 0.3 V. The SD_{Mass} values calculated by determination of stripping charges (SI Fig. S5 and Table S3) are shown in Figure 6 (a) displaying comparable values for Fe-N-ox-BP and Fe-N-aCoco and a slightly lower SD_{Mass} value for Fe-N-aRS. This can directly be related to the bulk amount of iron detected by ICP-MS, which was 0.1 wt% lower for Fe-N-aRS (see 3.1). With a look to the area-based site densities in Figure 6 (b) comparable site densities for the three catalysts are achieved when the BET surface area is used

for the calculation. If the external site density, which excludes micropores, is used, significantly higher values for the Fe-N-ox-BP catalyst can be found. This is due to the lower external surface area of Fe-N-ox-BP. Malko *et al.* used the external surface area with the assumption that micropores might not be electrochemical accessible, whereas Primbs *et al.* used the BET surface area for their calculations.^{35, 38} The SD_{BET} show comparable values and might be more suitable because the mass activities and the determined iron contents are highly comparable for all three catalysts which would also explain comparable site density.

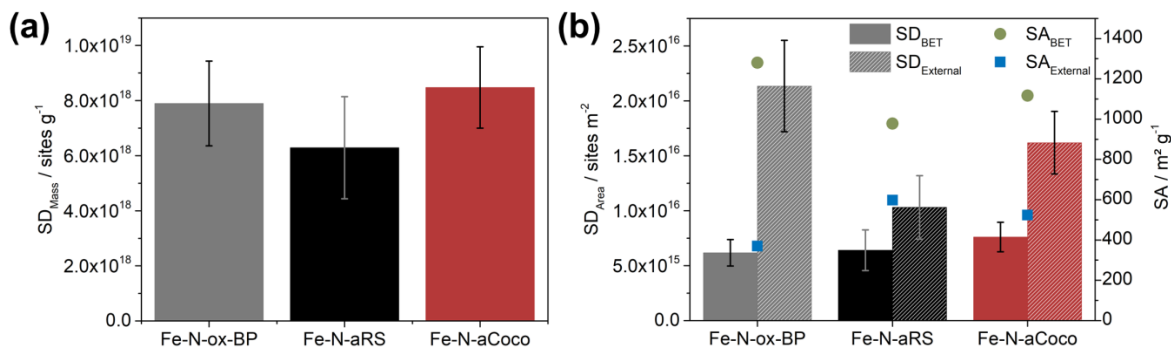


Figure 6. Calculated mass-based site densities (a) and area-based site densities using external surface area and BET surface area (b).

For determination of the TOF, the difference of kinetic activity ΔI_{kin} at 0.8 V before and after poisoning is used according to eq. 5.³⁸ This difference in kinetic current is calculated using the ORR curves in Figure 7 (a). By comparing the polarisation curves of all three catalysts, less negative values for the diffusion-limiting current densities compared to the ORR curves performed in 0.1 M $HClO_4$ are observed. Furthermore, the catalysts show higher current densities in the kinetic-limited region. Comparing the kinetic current densities at 0.8 V in 1 M $HClO_4$ with the j_{kin} values in 0.5 M acetate buffer an increase of factor 1.3 for both, Fe-N-aRS and Fe-N-aCoco and a factor of 2.7 for Fe-N-ox-BP are observed (see SI Table S4). Especially, the Fe-N-ox-BP catalyst

shows a significant increase in activity in acetate buffer compared to the measurements in HClO₄. Holst-Olesen *et al.* recently showed that the carboxyl species in acetate buffer can boost the ORR activity of Fe-N₄ sites in Fe-N-C catalysts by factor four compared to 0.1 M HClO₄ electrolyte.⁷⁰ They postulated that the carboxyl species (COOH/COO⁻) act as a competing adsorbate on the Fe atom in Fe-N₄ site leading to a stabilization of the initial and final state of the ORR cycle and thus leading to a decrease in overpotential and an increase of activity.⁷⁰ As the SD_{Mass} value and the mass activity in 0.1 M HClO₄ are comparable for all three catalysts the reason for the significantly higher activity of Fe-N-ox-BP in acetate buffer originates either from the nature of active sites or from the interaction between the electrolyte and the carbon structure. The biomass-based catalysts possess another electronic structure due to the phosphor species and higher N-doping which might hinder the adsorption of acetates on the active sites. This observation further underlines the differences in the carbon network structure of the biomass- and Back Pearl[®]-based catalysts.

The activity differences before and after poisoning in Figure 7 (b) show, that the Fe-N-ox-BP catalyst is more affected by the nitrite leading to nearly 50 % higher ΔI_{kin} values. This affects the TOF, leading to higher values for the Fe-N-ox-BP catalyst compared to the biomass-based catalysts in Figure 7 (c). Differences in nitrite poisoning due to different morphology and porosity can be excluded as the site densities which are used for the calculation of TOF (eq. 11) are in the same range. Furthermore, Primbs *et al.* performed nitrite stripping for catalysts with different micro- and mesoporosity and surface areas in the range of 463 m²/g to 840 m²/g, where no comparable behaviour to this study was observed.³⁵ Thus, the differences in the effect of poisoning must have other origins. Choi. *et al.* reported that oxygen functionalities on the carbon surface lead to electron-withdrawing from the Fe-site which decreases the O₂ binding for ORR and leads to a decreased activity and TOF.⁹ Although a higher amount of surface oxygen was found for the

biomass-based catalysts, comparable activities in HClO_4 were achieved. Furthermore, it can be assumed that the increased activity of the Fe-N-ox-BP in acetate buffer leads also to a stronger effect of poisoning which is not the case for the biomass-based catalyst. Therefore the final TOF values might not be reliable. Nevertheless, the nitrite stripping revealed comparable site densities for the catalysts and further indicate differences in the electronic structure of carbon support influenced by the phosphor species and higher N-content which led to higher stability of the Fe-N site against degradation via carbon corrosion.

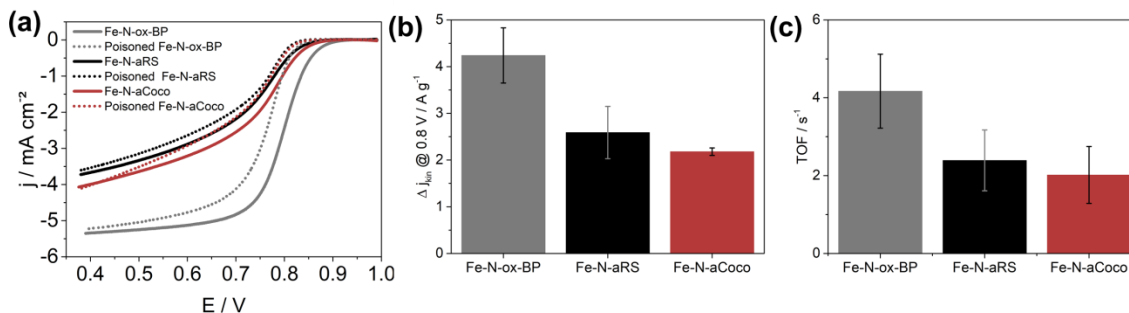


Figure 7. Polarisation curve before and after poisoning with nitrite (a), difference of kinetic current at 0.8 V before and after poisoning (b) and turnover frequency for the three Fe-N-C catalysts (c).

4. CONCLUSION

In summary, two Fe-N-C catalysts based on phosphoric acid activated biomasses were compared with a common Black Pearls[®]-based catalyst in terms of ORR activity, selectivity and stability in acidic electrolyte. Comparable ORR mass activities and site densities were achieved. A lower selectivity of the biomass-based Fe-N-C catalysts was observed which was correlated to the higher amount of nitrogen and especially pyrrolic nitrogen functionalities. In spite of the lower selectivity the biomass-based Fe-N-C catalysts show higher stability with up to 50 % less mass activity loss

during potential cycling between 1.0-1.5 V provoking electrochemical carbon corrosion. This significant higher stability was assigned to the phosphor species and higher content of N-functionalities especially pyrrolic nitrogen species in the biomass-based Fe-N-C catalysts. The electron-donating effect of P causes a higher stability of the functionalized carbon matrix near the active Fe-N site. Furthermore, the differences in surface structure between common Fe-N-C and biomass-based Fe-N-C catalysts were verified by different adsorption behavior of carboxylic groups observed in nitrite stripping experiments. Thus, this study documents the advantageous use of activated biomasses in Fe-N-C catalysts and suggests developing strategies for improving the carbon matrix durability for Fe-N site stabilization by introducing phosphor species.

ASSOCIATED CONTENT

Supporting Information

XP spectra of Fe-N-aCoco; N₂ sorption isotherms; ORR polarization curves of aRS and ox-BP; IL-TEM images of Fe-N-ox-BP; Nitrite stripping experiment curves; Table with porosity data; Table with capacities; Table with nitrite stripping experiment data; Table with mass activities in 0.1 M HClO₄ and 0.5 M acetate buffer; Discussion of influence of Pt-contamination by counter electrode.

AUTHOR INFORMATION

Corresponding Author

Julia Müller-Hülstede - Institute of Engineering Thermodynamics, German Aerospace Center (DLR), Carl-von-Ossietzky-Str. 15, 26129, Oldenburg, Germany; Institute of Chemistry, Carl von Ossietzky University, Carl-von-Ossietzky Str. 9-11, 26129, Oldenburg, Germany

Email: Julia.huelstede@dlr.de

Authors

Dana Schonvogel - Institute of Engineering Thermodynamics, German Aerospace Center (DLR),
Carl-von-Ossietzky-Str. 15, 26129, Oldenburg, Germany

Henrike Schmies - Institute of Engineering Thermodynamics, German Aerospace Center (DLR),
Carl-von-Ossietzky-Str. 15, 26129, Oldenburg, Germany

Peter Wagner - Institute of Engineering Thermodynamics, German Aerospace Center (DLR),
Carl-von-Ossietzky-Str. 15, 26129, Oldenburg, Germany

Alexander Dyck - Institute of Networked Energy Systems, German Aerospace Center (DLR),
Carl-von-Ossietzky-Str. 15, 26129, Oldenburg, Germany

Michael Wark - Institute of Chemistry, Carl von Ossietzky University, Carl-von-Ossietzky-Str.
9-11, 26129, Oldenburg, Germany

Notes

The authors declare no competing financial interest.

ACKNOWLEDGMENTS

This research was funded by Federal Ministry for Economic Affairs and Energy on the basis of a decision by the German Bundestag, grant number 03ETB016A. The XPS and XRD instruments are funded by DFG through grant INST 184/144-1 FUGG and INST 184/154-1 FUGG. We would like to thank Frank Schröter, Marco Weers (University Oldenburg) for the support in sorption experiments and Nina Bengen (DLR) for the support in ICP-MS measurements. The authors acknowledge the Electron and Light Microscopy Service Unit,

especially Ute Friedrich (Carl von Ossietzky University of Oldenburg) for the use of the imaging facilities.

REFERENCES

1. Wang, Y.; Ruiz Diaz, D. F.; Chen, K. S.; Wang, Z.; Adroher, X. C., Materials, technological status, and fundamentals of PEM fuel cells – A review. *Materials Today* **2020**, *32*, 178-203.
2. Zeis, R., Materials and characterization techniques for high-temperature polymer electrolyte membrane fuel cells. *Beilstein journal of nanotechnology* **2015**, *6*, 68-83.
3. Martinez, U.; Komini Babu, S.; Holby, E. F.; Chung, H. T.; Yin, X.; Zelenay, P., Progress in the Development of Fe-Based PGM-Free Electrocatalysts for the Oxygen Reduction Reaction. *Advanced materials* **2019**, *31* (31), e1806545.
4. Jaouen, F.; Jones, D.; Coutard, N.; Artero, V.; Strasser, P.; Kucernak, A., Toward Platinum Group Metal-Free Catalysts for Hydrogen/Air Proton-Exchange Membrane Fuel Cells. *Johnson Matthey Technology Review* **2018**, *62* (2), 231-255.
5. Osmieri, L., Transition Metal–Nitrogen–Carbon (M–N–C) Catalysts for Oxygen Reduction Reaction. Insights on Synthesis and Performance in Polymer Electrolyte Fuel Cells. *ChemEngineering* **2019**, *3* (1), 16.
6. Martinaiou, I.; Shahraei, A.; Grimm, F.; Zhang, H.; Wittich, C.; Klemenz, S.; Dolique, S. J.; Kleebe, H.-J.; Stark, R. W.; Kramm, U. I., Effect of metal species on the stability of Me-N-C catalysts during accelerated stress tests mimicking the start-up and shut-down conditions. *Electrochimica Acta* **2017**, *243*, 183-196.
7. Shao, Y.; Dodelet, J. P.; Wu, G.; Zelenay, P., PGM-Free Cathode Catalysts for PEM Fuel Cells: A Mini-Review on Stability Challenges. *Advanced materials* **2019**, *31* (31), e1807615.
8. Baricci, A., ; Bisello, A.; Serov, A.; Odgaard, M.; Atanassov, P.; Casalegno, A., Analysis of the effect of catalyst layer thickness on performance and durability of platinum group metal-free catalysts for polymer electrolyte membrane fuel cells. *Sustainable Energy & Fuels* **2019**, *3*, 3375-3386.
9. Choi, C.-H.; Lim, H.-K.; Chon, G.; Chung, M. W.; Altin, A.; Sahraie, N. R.; Sougrati, M.-T.; Stievano, L.; Oh, H. S.; Park, E. S.; Luo, F.; Strasser, P.; Drazic, G.; Kim, H.; Jaouen, F., Achilles' heel of Iron-Based Catalysts During Oxygen Reduction in Acidic Medium. *Energy & Environmental Science* **2018**, *11*, 3176-3182.
10. Kumar, K.; Dubau, L.; Mermoux, M.; Li, J.; Zitolo, A.; Nelayah, J.; Jaouen, F.; Maillard, F., On the Influence of Oxygen On the Degradation of Fe-N-C Catalysts. *Angew. Chem. Int. Ed.* **2019**, *59* (8), 3235-3243.
11. Ball, S. C.; Hudson, S. L.; Thompsett, D.; Theobald, B., An investigation into factors affecting the stability of carbons and carbon supported platinum and platinum/cobalt alloy catalysts during 1.2V potentiostatic hold regimes at a range of temperatures. *Journal of Power Sources* **2007**, *171* (1), 18-25.
12. Li, H.; Cheng, N.; Zheng, Y.; Zhang, X.; Lv, H.; He, D.; Pan, M.; Kleitz, F.; Qiao, S. Z.; Mu, S., Oxidation Stability of Nanographite Materials. *Advanced Energy Materials* **2013**, *3* (9), 1176-1179.

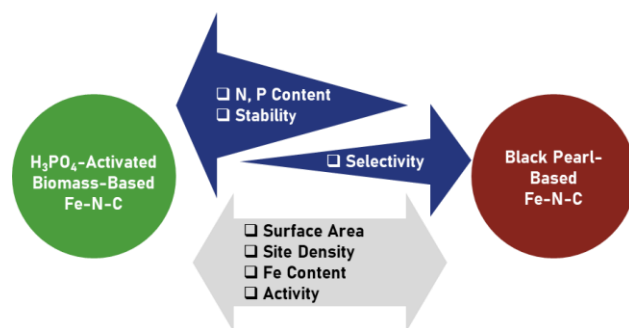
13. Goellner, V.; Baldizzone, C.; Schuppert, A.; Sougrati, M. T.; Mayrhofer, K.; Jaouen, F., Degradation of Fe/N/C catalysts upon high polarization in acid medium. *Physical chemistry chemical physics : PCCP* **2014**, *16* (34), 18454-62.
14. Leonard, N.; Nallathambi, V.; Barton, S. C., Carbon Supports for Non-Precious Metal Oxygen Reducing Catalysts. *Journal of The Electrochemical Society* **2013**, *160* (8), F788-F792.
15. Wu, G.; More, K. L.; Xu, P.; Wang, H. L.; Ferrandon, M.; Kropf, A. J.; Myers, D. J.; Ma, S.; Johnston, C. M.; Zelenay, P., A carbon-nanotube-supported graphene-rich non-precious metal oxygen reduction catalyst with enhanced performance durability. *Chemical communications* **2013**, *49* (32), 3291-3.
16. Fu, X.; Hassan, F. M.; Zamani, P.; Jiang, G.; Higgins, D. C.; Choi, J.-Y.; Wang, X.; Xu, P.; Liu, Y.; Chen, Z., Engineered architecture of nitrogenous graphene encapsulating porous carbon with nano-channel reactors enhancing the PEM fuel cell performance. *Nano Energy* **2017**, *42*, 249-256.
17. Xu, Z.; Ma, J.; Shi, M.; Xie, Y.; Feng, C., Biomass based iron and nitrogen co-doped 3D porous carbon as an efficient oxygen reduction catalyst. *Journal of colloid and interface science* **2018**, *523*, 144-150.
18. Zhang, J.; Wu, S.; Chen, X.; Cheng, K.; Pan, M.; Mu, S., An animal liver derived non-precious metal catalyst for oxygen reduction with high activity and stability. *RSC Advances* **2014**, *4* (62), 32811.
19. Guo, C.-Z.; Liao, W.-L.; Chen, C.-G., Design of a non-precious metal electrocatalyst for alkaline electrolyte oxygen reduction by using soybean biomass as the nitrogen source of electrocatalytically active center structures. *Journal of Power Sources* **2014**, *269*, 841-847.
20. Wang, K.; Wang, H.; Ji, S.; Feng, H.; Linkov, V.; Wang, R., Biomass-derived activated carbon as high-performance non-precious electrocatalyst for oxygen reduction. *RSC Advances* **2013**, *3* (30), 12039.
21. Zhang, X.; Liu, R.; Zang, Y.; Liu, G.; Liu, S.; Wang, G.; Zhang, Y.; Zhang, H.; Zhao, H., Shrimp-shell derived carbon nanodots as precursors to fabricate Fe,N-doped porous graphitic carbon electrocatalysts for efficient oxygen reduction in zinc-air batteries. *Inorganic Chemistry Frontiers* **2016**, *3* (7), 910-918.
22. Liu, Y.; Su, M.; Li, D.; Li, S.; Li, X.; Zhao, J.; Liu, F., Soybean straw biomass-derived Fe-N co-doped porous carbon as an efficient electrocatalyst for oxygen reduction in both alkaline and acidic media. *RSC Advances* **2020**, *10* (12), 6763-6771.
23. Chen, Q.; Tan, X.; Liu, Y.; Liu, S.; Li, M.; Gu, Y.; Zhang, P.; Ye, S.; Yang, Z.; Yang, Y., Biomass-derived porous graphitic carbon materials for energy and environmental applications. *Journal of Materials Chemistry A* **2020**, *8* (12), 5773-5811.
24. Elmouwahidi, A.; Bailon-Garria, E.; Perez-Cadenas, A. F.; Maldonado-Hodar, F. J.; Carrasco-Marin, F., Activated carbons from KOH and H3P04-activation of olive residues and its application as supercapacitor electrodes. *Electrochimica Acta* **2017**, *229*, 219-228.
25. Luo, Y.; Li, D.; Chen, Y.; Sun, X.; Cao, Q.; Liu, X., The performance of phosphoric acid in the preparation of activated carbon-containing phosphorus species from rice husk residue. *Journal of Materials Science* **2018**, *54* (6), 5008-5021.
26. Wang, Y.; Zuo, S.; Miao, M.; Liu, Y.; Gu, Z.; Jin, Y., Cost-effective preparation of metal-free electrocatalysts by phosphoric acid activation of lignocellulosic materials for oxygen reduction reaction. *International Journal of Hydrogen Energy* **2019**, *44* (5), 2811-2822.
27. Borghei, M.; Laocharoen, N.; Kibena-Pöldsepp, E.; Johansson, L.-S.; Campbell, J.; Kauppinen, E.; Tammeveski, K.; Rojas, O. J., Porous N,P-doped carbon from coconut shells

- with high electrocatalytic activity for oxygen reduction: Alternative to Pt-C for alkaline fuel cells. *Applied Catalysis B: Environmental* **2017**, *204*, 394-402.
28. Volperts, A.; Plavniece, A.; Dobeles, G.; Zhurinskis, A.; Kruusenberg, I.; Kaare, K.; Locs, J.; Tamasauskaitė-Tamasiunaite, L.; Norkus, E., Biomass based activated carbons for fuel cells. *Renewable Energy* **2019**, *141*, 40-45.
 29. Hülstede, J.; Schonvogel, D.; Schmies, H.; Wagner, P.; Schröter, F.; Dyck, A.; Wark, M., Relevant Properties of Carbon Support Materials in Successful Fe-N-C Synthesis for the Oxygen Reduction Reaction: Study of Carbon Blacks and Biomass-Based Carbons. *Materials* **2021**, *14* (1), 45.
 30. Koyuturk, B.; Evans, J.; Mulhaupt, H.; Selve, S.; Simke, J. R. J.; Wark, M.; Feller, T. P., Sol-gel chemistry in molten Brønsted acids towards "activated" carbons and beyond. *Nanoscale* **2019**, *11* (27), 13154-13160.
 31. Schmies, H.; Hornberger, E.; Anke, B.; Jurzinsky, T.; Nong, H. N.; Dionigi, F.; Kühl, S.; Drnec, J.; Lerch, M.; Cremers, C.; Strasser, P., Impact of Carbon Support Functionalization on the Electrochemical Stability of Pt Fuel Cell Catalysts. *Chemistry of Materials* **2018**, *30* (20), 7287-7295.
 32. Chung, H. T.; Johnston, C. M.; Artyushkova, K.; Ferrandon, M.; Myers, D. J.; Zelenay, P., Cyanamide-derived non-precious metal catalyst for oxygen reduction. *Electrochemistry Communications* **2010**, *12* (12), 1792-1795.
 33. Tian, J.; Birry, L.; Jaouen, F.; Dodelet, J. P., Fe-based catalysts for oxygen reduction in proton exchange membrane fuel cells with cyanamide as nitrogen precursor and/or pore-filler. *Electrochimica Acta* **2011**, *56* (9), 3276-3285.
 34. Wu, G.; More, K. L.; Johnston, C. M.; Zelenay, P., High-performance electrocatalysts for oxygen reduction derived from polyaniline, iron, and cobalt. *Science* **2011**, *332* (6028), 443-7.
 35. Primbs, M.; Sun, Y.; Roy, A.; Malko, D.; Mehmood, A.; Sougrati, M.-T.; Blanchard, P.-Y.; Granozzi, G.; Kosmala, T.; Daniel, G.; Atanassov, P.; Sharman, J.; Durante, C.; Kucernak, A.; Jones, D.; Jaouen, F.; Strasser, P., Establishing reactivity descriptors for platinum group metal (PGM)-free Fe-N-C catalysts for PEM fuel cells. *Energy & Environmental Science* **2020**, *13* (8), 2480-2500.
 36. Ohmaa, A.; Shinoharaa, K.; Iiyamaa, A.; Yoshidab, T.; Daimaru, A., Membrane and Catalyst Performance Targets for Automotive Fuel Cells by FCCJ Membrane, Catalyst, MEA WG. *ECS Transaction* **2011**, *41* (1), 775-784.
 37. Marshall-Roth, T.; Libretto, N. J.; Wrobel, A. T.; Anderton, K. J.; Pegis, M. L.; Riche, N. D.; Voorhis, T. V.; Miller, J. T.; Surendranath, Y., A pyridinic Fe-N₄ macrocycle models the active sites in Fe/N-doped carbon electrocatalysts. *Nature communications* **2020**, *11* (1), 5283.
 38. Malko, D.; Kucernak, A.; Lopes, T., In situ electrochemical quantification of active sites in Fe-N/C non-precious metal catalysts. *Nature communications* **2016**, *7*, 13285.
 39. Einsle, O.; Messerschmidt, A.; Huber, R.; Kroneck, P. M. H.; Neese, F., Mechanism of the Six-Electron Reduction of Nitrite to Ammonia by Cytochrome c Nitrite Reductase. *J. Am. Soc.* **2002**, *124* (39), 11737-11745.
 40. Kruk, M.; Jaroniec, M.; Berenzitski, Y., Adsorption Study of Porous Structure Development in Carbon Blacks. *Journal of colloid and interface science* **1996**, *182*, 282-288.
 41. Osman, A. I.; Farrell, C.; Al-Muhtaseb, A. H.; Harrison, J.; Rooney, D. W., The production and application of carbon nanomaterials from high alkali silicate herbaceous biomass. *Scientific reports* **2020**, *10* (1), 2563.

42. Shrestha, D.; Maensiri, S.; Wongpratrat, U.; Lee, S. W.; Nyachhyon, A. R., Shorea robusta derived activated carbon decorated with manganese dioxide hybrid composite for improved capacitive behaviors. *Journal of Environmental Chemical Engineering* **2019**, 7 (5).
43. Wang, D.-W.; Su, D., Heterogeneous nanocarbon materials for oxygen reduction reaction. *Energy & Environmental Science* **2014**, 7 (2), 576.
44. Strelko, V. V., Role of carbon matrix heteroatoms at synthesis of carbons for catalysis and energy applications. *Journal of Energy Chemistry* **2013**, 22, 174-182.
45. Choi, C. H.; Park, S. H.; Woo, S. I., Phosphorus–nitrogen dual doped carbon as an effective catalyst for oxygen reduction reaction in acidic media: effects of the amount of P-doping on the physical and electrochemical properties of carbon. *Journal of Materials Chemistry* **2012**, 22 (24), 12107.
46. Artyushkova, K.; Serov, A.; Rojas-Carbonell, S.; Atanasov, P., Chemistry of Multitudinous Active Sites for Oxygen Reduction Reaction in Transition Metal–Nitrogen–Carbon Electrocatalysts. *The Journal of Physical Chemistry C* **2015**, 119 (46), 25917-25928.
47. Uddin, A.; Dunsmore, L.; Zhang, H.; Hu, L.; Wu, G.; Litster, S., High Power Density Platinum Group Metal-free Cathodes for Polymer Electrolyte Fuel Cells. *ACS applied materials & interfaces* **2020**, 12 (2), 2216-2224.
48. Bonakdarpour, A.; Lefevre, M.; Yang, R.; Jaouen, F.; Dahn, T.; Dodelet, J.-P.; Dahn, J. R., Impact of Loading in RRDE Experiments on Fe–N–C Catalysts: Two- or Four-Electron Oxygen Reduction? *Electrochemical and Solid-State Letters* **2008**, 11 (6), B105.
49. Kumar, K.; Asset, T.; Li, X.; Liu, Y.; Yan, X.; Chen, Y.; Mermoux, M.; Pan, X.; Atanasov, P.; Maillard, F.; Dubau, L., Fe–N–C Electrocatalysts' Durability: Effects of Single Atoms' Mobility and Clustering. *ACS Catalysis* **2021**, 11 (2), 484-494.
50. Shinagawa, T.; Garcia-Esparza, A. T.; Takanabe, K., Insight on Tafel slopes from a microkinetic analysis of aqueous electrocatalysis for energy conversion. *Scientific reports* **2015**, 5, 13801.
51. Osmieri, L.; Monteverde Videla, A. H. A.; Ocón, P.; Specchia, S., Kinetics of Oxygen Electroreduction on Me–N–C (Me = Fe, Co, Cu) Catalysts in Acidic Medium: Insights on the Effect of the Transition Metal. *The Journal of Physical Chemistry C* **2017**, 121 (33), 17796-17817.
52. Sgarbi, R.; Kumar, K.; Jaouen, F.; Zitolo, A.; Ticianelli, E. A.; Maillard, F., Oxygen reduction reaction mechanism and kinetics on M-NxCy and M@N-C active sites present in model M-N-C catalysts under alkaline and acidic conditions. *Journal of Solid State Electrochemistry* **2019**, 45-56.
53. Schardt, S.; Weidler, N.; Wallace, W.; Martinaiou, I.; Stark, R.; Kramm, U., Influence of the Structure-Forming Agent on the Performance of Fe-N-C Catalysts. *Catalysts* **2018**, 8 (7), 260.
54. Luo, F.; Roy, A.; Silvioli, L.; Cullen, D. A.; Zitolo, A.; Sougrati, M. T.; Oguz, I. C.; Mineva, T.; Teschner, D.; Wagner, S.; Wen, J.; Dionigi, F.; Kramm, U. I.; Rossmeisl, J.; Jaouen, F.; Strasser, P., P-block single-metal-site tin/nitrogen-doped carbon fuel cell cathode catalyst for oxygen reduction reaction. *Nature materials* **2020**, 19, 1215-1223.
55. Shao-Horn, Y.; Sheng, W. C.; Chen, S.; Ferreira, P. J.; Holby, E. F.; Morgan, D., Instability of Supported Platinum Nanoparticles in Low-Temperature Fuel Cells. *Topics in Catalysis* **2007**, 46 (3-4), 285-305.

56. Choi, C. H.; Baldizzone, C.; Grote, J. P.; Schuppert, A. K.; Jaouen, F.; Mayrhofer, K. J., Stability of Fe-N-C Catalysts in Acidic Medium Studied by Operando Spectroscopy. *Angewandte Chemie* **2015**, *54* (43), 12753-7.
57. Kumar, K.; Gairola, P.; Lions, M.; Ranjbar-Sahraie, N.; Mermoux, M.; Dubau, L.; Zitolo, A.; Jaouen, F.; Maillard, F., Physical and Chemical Considerations for Improving Catalytic Activity and Stability of Non-Precious-Metal Oxygen Reduction Reaction Catalysts. *ACS Catalysis* **2018**, *8* (12), 11264-11276.
58. Kramm, U. I.; Zana, A.; Vosch, T.; Fiechter, S.; Arenz, M.; Schmeißer, D., On the structural composition and stability of Fe-N-C catalysts prepared by an intermediate acid leaching. *Journal of Solid State Electrochemistry* **2015**, *20* (4), 969-981.
59. Bae, G.; Chung, M. W.; Ji, S. G.; Jaouen, F.; Choi, C. H., pH Effect on the H₂O₂-Induced Deactivation of Fe-N-C Catalysts. *ACS Catalysis* **2020**, *10* (15), 8485-8495.
60. Li, J.; Ghoshal, S.; Liang, W.; Sougrati, M.-T.; Jaouen, F.; Halevi, B.; McKinney, S.; McCool, G.; Ma, C.; Yuan, X.; Ma, Z.-F.; Mukerjee, S.; Jia, Q., Structural and mechanistic basis for the high activity of Fe-N-C catalysts toward oxygen reduction. *Energy & Environmental Science* **2016**, *9* (7), 2418-2432.
61. Li, J.; Alsudairi, A.; Ma, Z. F.; Mukerjee, S.; Jia, Q., Asymmetric Volcano Trend in Oxygen Reduction Activity of Pt and Non-Pt Catalysts: In Situ Identification of the Site-Blocking Effect. *Journal of the American Chemical Society* **2017**, *139* (4), 1384-1387.
62. Li, J.; Jia, Q.; Mukerjee, S.; Sougrati, M.-T.; Drazic, G.; Zitolo, A.; Jaouen, F., The Challenge of Achieving a High Density of Fe-Based Active Sites in a Highly Graphitic Carbon Matrix. *Catalysts* **2019**, *9* (2), 144.
63. Jaouen, F.; Herranz, J.; Lefevre, M.; Dodelet, J. P.; Kramm, U. I.; Herrmann, I.; Bogdanoff, P.; Maruyama, J.; Nagaoka, T.; Garsuch, A.; Dahn, J. R.; Olson, T.; Pylypenko, S.; Atanassov, P.; Ustinov, E. A., Cross-laboratory experimental study of non-noble-metal electrocatalysts for the oxygen reduction reaction. *ACS applied materials & interfaces* **2009**, *1* (8), 1623-39.
64. Zana, A.; Speder, J.; Reeler, N. E. A.; Vosch, T.; Arenz, M., Investigating the corrosion of high surface area carbons during start/stop fuel cell conditions: A Raman study. *Electrochimica Acta* **2013**, *114*, 455-461.
65. Kim, Y.-T.; Ito, Y.; Tadaï, K.; Mitani, T., Drastic change of electric double layer capacitance by surface functionalization of carbon nanotubes. *Appl. Phys. Lett.* **2005**, *87*, 234106.
66. Kübler, M.; Wagner, S.; Jurzinsky, T.; Paul, S.; Weidler, N.; Gomez Villa, E. D.; Cremers, C.; Kramm, U. I., Impact of Surface Functionalization on the Intrinsic Properties of the Resulting Fe-N-C Catalysts for Fuel Cell Applications. *Energy Technology* **2020**, *8* (9), 2000433.
67. Li, J.; Sougrati, M. T.; Zitolo, A.; Ablett, J. M.; Oğuz, I. C.; Mineva, T.; Matanovic, I.; Atanassov, P.; Huang, Y.; Zenyuk, I.; Di Cicco, A.; Kumar, K.; Dubau, L.; Maillard, F.; Dražić, G.; Jaouen, F., Identification of durable and non-durable FeN_x sites in Fe-N-C materials for proton exchange membrane fuel cells. *Nature Catalysis* **2020**, *4*, 10-19.
68. Li, Y.; Li, J.; Wang, Y.-G.; Chen, X.; Liu, M.; Zheng, Z.; Peng, X., Carbon corrosion mechanism on nitrogen-doped carbon support - A density functional theory study. *International Journal of Hydrogen Energy* **2021**, *46*, 13273-13282.
69. Shen, H.; Thomas, T.; Rasaki, S. A.; Saad, A.; Hu, C.; Wang, J.; Yang, M., Oxygen Reduction Reactions of Fe-N-C Catalysts: Current Status and the Way Forward. *Electrochemical Energy Reviews* **2019**, *2* (2), 252-276.

70. Holst-Olesen, K.; Silvioli, L.; Rossmesl, J.; Arenz, M., Enhanced Oxygen Reduction Reaction on Fe/N/C Catalyst in Acetate Buffer Electrolyte. *ACS Catalysis* **2019**, 9 (4), 3082-3089.



For Table of Contents Only